Materials and Design 181 (2019) 108054

Contents lists available at ScienceDirect

Materials and Design

journal homepage: www.elsevier.com/locate/matdes

Melt pool controlled laser powder bed fusion for customised low-density lattice structures

Alexander Großmann[a,*], Julian Felger[b], Tilman Frölich[a], Julian Gosmann[a], Christian Mittelstedt[a]

[a]Technical University Darmstadt Institute for Lightweight Construction and Design Otto-Berndt-Straße 2, Darmstadt 64287, Germany
[b]Technical University Darmstadt Institute of Structural Mechanics Franziska-Braun-Straße 7, Darmstadt 64287, Germany

GRAPHICAL ABSTRACT

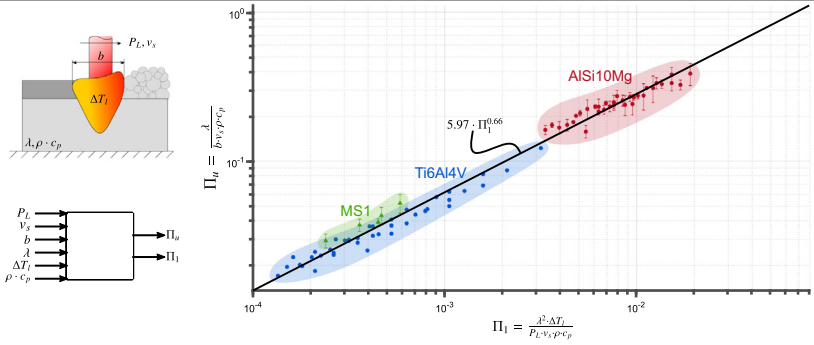

ARTICLE INFO

Article history:
Received 18 June 2019
Received in revised form 8 July 2019
Accepted 18 July 2019
Available online 30 July 2019

Keywords:
Lattice structures
Additive manufacturing
Laser powder bed fusion
Melt pool control
Melt pool characterization
Scaling laws

ABSTRACT

Laser powder bed fusion is a promising technology enabling the manufacturing of complex parts such as cellular structures with superior mechanical properties. However, their fabrication is not straightforward, since the geometry of the melt track and the constitution of the melt pool significantly affects the dimensions of the final part. Thus, a sound understanding of the interrelation between process parameters, the melting process and the geometry of the melt track is of crucial importance in order to ensure high quality of the lattice. In this work, a scaling law is proposed that relates the width of a single melt track to process and material parameters. This is done employing dimensional analysis as well as an averaged energy balance. The predictive power of the proposed model is demonstrated based on extensive experimental data provided by the authors. Considering truss lattices, the present approach bridges the gap between manufacturing parameters and macroscopic characteristics of lattice structures. This ultimately enables a proactive adjustment of process parameters in order to tailor the lattice's geometry and the elastic properties. Moreover, the proposed modelling approach serves as a basis for an extended theory accounting for additional physical effects present in selective laser melting.

1. Introduction

Laser powder bed fusion (LPBF) is a key enabler to manufacture open celled non-stochastic cellular structures, e.g. lattices that find applications such as medical implants, impact absorbers, heat exchangers, filters, acoustic absorbers and lightweight structures [3,8,11,25]. On the one hand, they have a high stiffness-to-weight ratio and a broad range of possible applications. On the other hand, LPBF is the most suitable technology to manufacture lattices. For this reason, many authors investigate the manufacturability and mechanical properties of these structures in the present LPBF related

* Corresponding author.
E-mail address: alexander.grossmann@klub.tu-darmstadt.de (A. Großmann).

https://doi.org/10.1016/j.matdes.2019.108054

literature [2,5–7,16,19,25,26,30–33]. For LPBF parts such as thin-walled lattice structures the melt track is the structure determining quantity defining not only the structure's macroscopic but also its mesoscopic properties [4,20,23,27,35], e.g. the porosity. In addition, the melt pool properties highly impact the microstructure which is particularly pronounced for thin-walled lattice structures where an elongated grain morphology is observed [22,29]. Thus, a sound characterization of the melting process is of crucial importance to guarantee controllability and quality of the manufactured lattice structure. However, the LPBF process is complex since numerous physical phenomena are involved, for instance Marangoni convection [13], laser-powder interaction, heat conduction, melting and re-solidification processes, gravitational effects or a highly dynamic melt pool, among others. Moreover, several undesired side effects may occur e.g. a high surface tension gradient in the melt pool leads to splashes during the process and to pores in the final part. Therefore, it is essential to have a qualitative and quantitative understanding to which extent process parameters such as the laser power P_L and the scanning speed v_s are interrelated with these physical mechanisms defining the constitution of the melt pool. A mathematical and physically sound relation between melt pool width and material as well as process parameters is thus most desirable.

In LPBF, there are numerous parameters influencing the quality of the final part [25]. With respect to single track many authors investigate the correlation between process parameters and melt pool behavior. Essentially, there are two approaches to characterize the interdependence between process parameters and melt pool behavior: descriptive approaches employing experimental data to deduce an empirical process window and identify suitable combinations of laser power and scan speed [4,9,10,14,17,24]. Alternatively, there is a predictive approach relying on extensive numerical simulations to investigate the laser melting process [12,13,15,36,37]. Kolossov et al. [15] solved a three-dimensional, non-linear, transient heat transfer problem using the finite-element method (FEM). Xiao and Zhang [37] proposed a numerical model of the convection-diffusion phase-change process during laser melting employing the finite-volume method (FVM). Here, melting and re-solidification of a direct metal laser melting process have been modelled taking into account effects of shrinkage and natural convection driven by surface tension and buoyancy force. Wei et al. combined the FVM assuming laminar flow with a discrete element method (DEM) [36]. The effect of the laser power and the laser scanning speed on the thermodynamic behavior of the melt pool has been examined considering temperature dependent material properties such as thermal conductivity, viscosity and density.

All the previously mentioned numerical approaches share a high degree of complexity accounting for an increasing number of physical effects. However, resolving finer and finer physical scales, for instance time and length scales associated to turbulence phenomena within the melting zone, is accompanied with serious shortcomings. The most prominent are a high numerical effort and a huge number of input variables which are naturally fraught with uncertainties. A simple predictive physical model connecting the basic manufacturing input parameters with the final output parameters is still an open problem.

In this work, the authors propose a simple, coarse grained model which allows for describing the melt pool's width b with respect to the most important process parameters, that is, laser power P_L and scanning speed v_s as well as material parameters of the powder. The two independent approaches of dimensional analysis as well as averaged energy balance in integral form are used to independently derive the following scaling law implying self-similarity of the melting process: the width b of the melt pool scales with the square-root of the line energy E_L, that denotes the laser power P_L divided by the scanning speed v_s

$$E_L = \frac{P_L}{v_s}. \tag{1}$$

Additionally, the diameter d of an individual strut of the lattice obeys the same scaling law, cf. Fig. 1 C. An extensive data set composed of the powder alloys aluminum AlSi10Mg, titanium Ti6Al4V and maraging steel 1.2709 is generated in order to experimentally validate the proposed model. In a previous work provided by the authors, a homogenisation approach has been used to relate the strut diameter and orientation to the effective macroscopic elastic properties of a representative lattice volume element, cf. Fig. 1 A and B [28]. Combining homogenisation with the scaling law proposed in the present work bridges the gap between process parameters on the one hand and geometry and elastic properties of the lattice structure on the other hand. Consequently, adjusting the melt pool

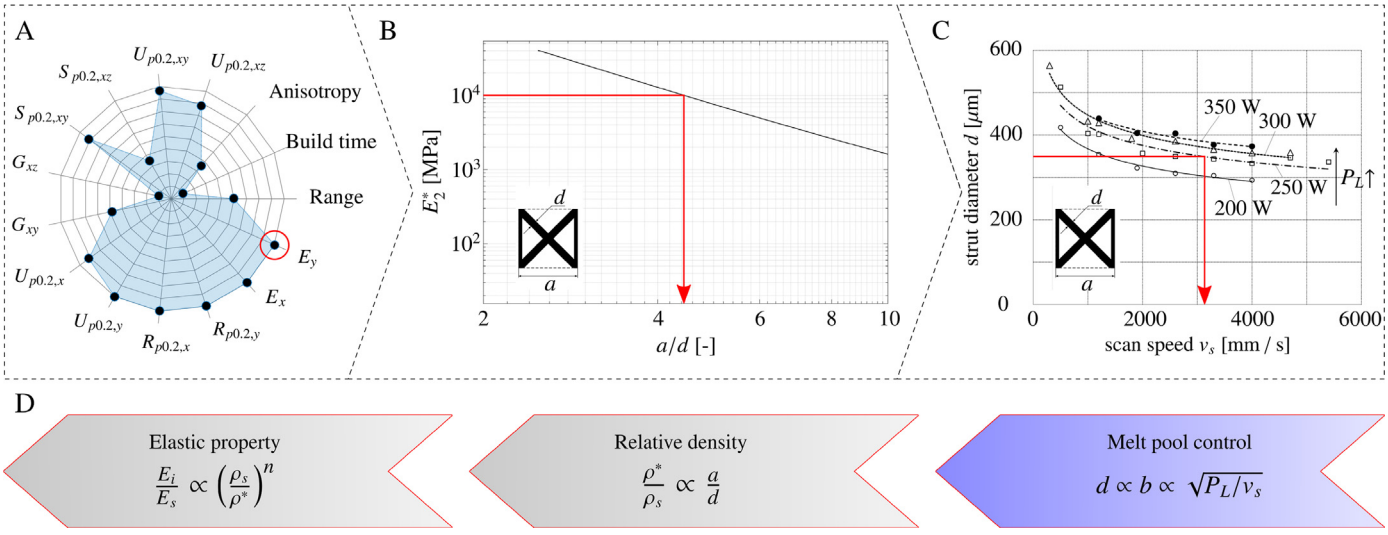

Fig. 1. Design concept for lattice structures in LPBF. (A) Schematic spider plot to assess the mechanical properties of a selected lattice. (B) Mechanical property E_2 with respect to the aspect ratio a/d for a 316L f2ccz lattice. (C) Correlation between lattice strut diameter d and process parameters laser power P_L and scan speed v_s for contour exposure (A–C according to previous work by the authors) [28] (D) Schematic description of correlation between process parameters and elastic properties.

width directly controls the mechanical properties of the lattice which facilitates manufacturing significantly. Despite truss lattices, the presented model is holistic in a sense that it serves as a basis for manufacturing further types of low density lattice structures presented in literature such as recoverable lattices [19], plate-lattices [30] or hierarchical lattice structures [6].

2. Preliminary experimental investigation

In order to develop a basic understanding of the interrelation between process parameters, lattice geometry, quality of the lattice and the dominant physical mechanism occurring during melting process, experimental data has been generated by the authors. Initially, the effect of process parameters on the visual surface quality of the lattice is considered. According to Fig. 2 A, a significant impact of the process parameters laser power P_L and scan speed v_s on the resulting strut diameter d is observed. The lattices have been manufactured employing contour exposure strategy and holding the CAD strut diameter fix at $d_{CAD} = 100\mu m$. Increasing the laser power or decreasing the scanning speed leads to an increase in strut diameter. Thus, the melt pool ultimately dictates the dimensions of the individual struts of which the lattice structure is composed (cf. Fig. 1). This illustrates that having a mathematical model at hand describing the width of the melt pool in terms of process and material parameters is of crucial importance to actively control the manufacturing process according to the desired macroscopic characteristics of the lattice, such as the effective stiffness. To further specify the dominant physical effects which are of practical importance, a so-called process window is deduced empirically, as shown in Fig. 2 B. Similar approaches are carried out throughout the literature experimentally and numerically using different materials, e.g. by Buchbinder et al. [4], Gong et al. [9] or Wei et al. [36]. The assignability for truss lattice structures is rarely regarded in the present literature. Thus, numerous truss lattice structures have been manufactured employing AlSi10Mg material, a typical aluminum alloy for LPBF. For high line energies $E_L = P_L/v_s > 0.25 J\,mm^{-1}$, a high level of energy is transferred into the powder bed. As depicted in Fig. 2 C(1), this results in high particle adhesion at the downskin surface, that is, the area where the normal vector of the surface is directed towards the build plate [34]. For very low line energies $E_L < 0.05 J\,mm^{-1}$, high surface tension gradients are present in the melt zone leading to balling, a phenomenon where no coherent melt track is produced [18]. Furthermore, above the laser power threshold $P_L \approx 340\,W$, high particle adhesion and pores are observed. Below the threshold $P_L \approx 180\,W$, the energy density transferred into the powder does not suffice to liquefy the powder. Exemplary illustrations of resultant surface qualities are depicted in Fig. 2 C–H.

3. Dimensional analysis

Dimensional analysis is a powerful tool to identify the governing quantities of a physical system such as the LPBF process. One famous example in the literature is the Reynolds number describing the ratio of inertia forces to viscous forces, representing a single quantity to characterize the transition from laminar to turbulent flow [38]. Thus, dimensional analysis allows for deriving simple physical relations for very complex phenomena without the necessity of modelling every detail of the considered process, as for instance demonstrated by G. I. Taylor approaching the problem of a nuclear explosion. However, at the outset of applying dimensional analysis, it is crucial to identify the correct governing physical quantities of the phenomenon under consideration [1]. Furthermore, dimensional analysis becomes inefficient the more physical parameters are considered. Thus, successfully applying dimensional analysis means to take as many as needed but as few as possible governing quantities into account. For these reasons, only the practically important region of the process

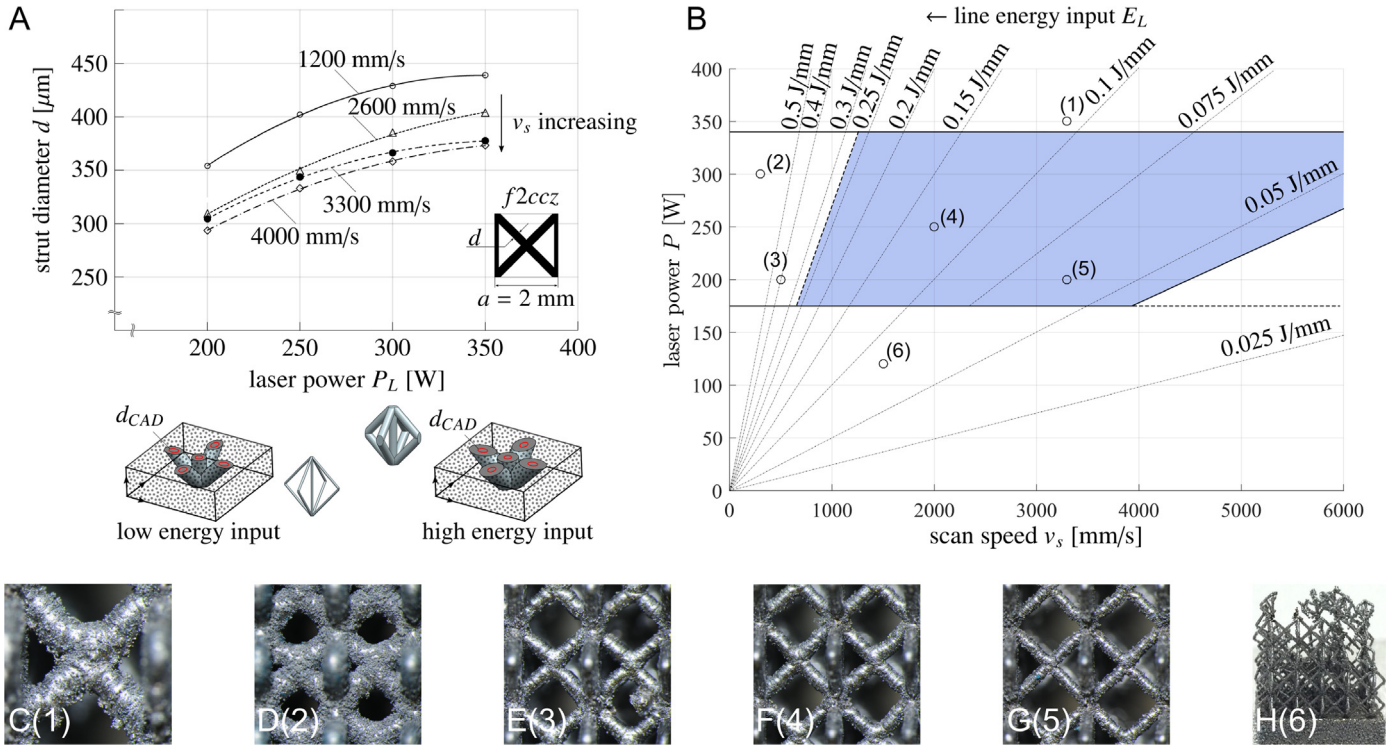

Fig. 2. Empirical data for LPBF of aluminum alloy AlSi10Mg (A) Correlation between structure diameter / melt pool width and process settings with CAD strut diameter of $d_{CAD} = 100\mu m$ (B) Process window denoting the structure's quality (C–H) Exemplary illustration of lattice surface quality for different process settings.

window is considered where a sound surface quality of the lattice is obtained according to the experimental data provided in Section 2. Consequently, undesired side effects associated to physical phenomena such as pronounced Marangoni convection, Plateau-Rayleigh instability and laser recoil pressure [13] are assumed to be negligible in the sense of a first order approximation. Further, the Laplace number La representing the ratio of inertia and capillary effects to viscous forces, takes high values, $La \approx 10^5$ for titanium Ti6Al4 V and aluminum AlSi10Mg. Thus during powder melting, viscous effects such as viscous heat dissipation are small and can be neglected. The melting process is modelled as quasi-stationary implying that the perspective of an observer attached to the laser moving with the laser velocity v_s is taken. Thus, time does not explicitly enter the problem as governing parameter. During melting, the laser beam energy is absorbed within the powder bed, the powder temperature increases, phase transformation from solid to liquid phase takes place and thermal energy spreads by heat diffusion.

Hence, according to Fig. 3, our governing parameters characterizing the melt pool width b are given by the scanning speed v_s, the laser power P_L, the change in temperature ΔT_l between initial and liquid state of the powder, the product of density and effective specific heat capacity $\rho \cdot c_p$ as well as the heat conductivity λ accounting for heat diffusion:

$$b = F(v_s, P_L, \Delta T_l, \rho \cdot c_p, \lambda). \tag{2}$$

A suitable fundamental system of dimensions is $[LMT\Theta]$ with length L, mass M, time T and temperature Θ. The dimensions of the quantities involved in Eq. (2) are systematically summarised in the dimension matrix presented in Table 1.

An essential property of Eq. (2) is its scale invariance: physical relations must be valid regardless of the underlying system of units that is employed in order to measure the individual dimension length, mass, time and temperature [1]. This fundamental statement represents the basis of the so-called Buckingham Π-theorem. It follows, that the physical relationship in Eq. (2) between the melt pool width b and the remaining governing parameters can be written equivalently as a relation between two dimensionless parameters Π_u and Π_1:

$$\Pi_u = f(\Pi_1). \tag{3}$$

The dimensionless parameters are given by:

$$\Pi_u = \frac{\lambda}{b v_s \rho c_p}, \quad \Pi_1 = \frac{\lambda^2 \Delta T_l}{P_L v_s \rho c_p}. \tag{4}$$

Thus, employing dimensional analysis reduces the number of involved quantities from six dimensional parameters to only two

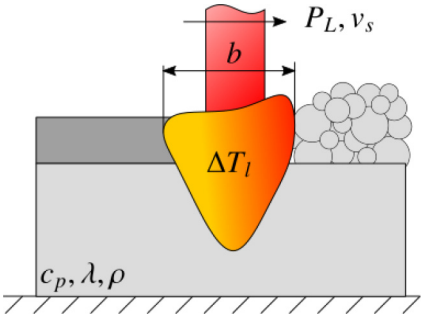

Fig. 3. Schematic of the melting process including governing parameters for dimensional analysis. A self-similar melt pool with circular cross section is assumed and b denotes maximum melt pool width.

Table 1
Dimensional table with the material and process specific input variables in an $[LMT\Theta]$-system.

	b	P_L	v_s	λ	$\rho \cdot c_p$	ΔT_l
L	1	2	1	1	-1	0
M	0	1	0	1	1	0
T	0	−3	−1	−3	−2	0
Θ	0	0	0	−1	−1	1

dimensionless parameters. Putting this slightly differently, Eq. (3) implies the following: Supposed there are data points of the melt pool width for different values of scanning speed and laser power. Plotted with respect to a Π_u-Π_1 coordinate system, all these data points must collapse to one single curve regardless of the used material. Here the coarse grained model neglects physical effects like radiation and re-solidification. Additionally, material and process specific quantities such as laser beam diameter, hatch distance, layer thickness, powder shape, diameter and absorptivity are neglected in this initial investigation. The objective is to keep the dimensional analysis as simple as possible and to consider only the most dominating quantities. Further investigations, however, will focus on assessing the influence of additional potential physical phenomena, process parameters and material properties.

4. Experimental details on melt pool characterization

4.1. Materials

In order to measure the melt pool width, experiments have been performed with aluminum AlSi10Mg and maraging steel 1.2709. Furthermore, experimental data from literature using Ti6A14 V is considered [9]. The relevant material properties are given in Table 2.

4.2. Single melt track specimens and measurements

Several undesired side effects can occur during manufacturing of the specimens such as warping [34] or build plate adhesion. To minimize these negative influences on the specimen geometry a preinvestigation has shown that the specimen geometry in Fig. 4 (a) shows the least side effects. Specimens with the approximate dimensions of 10 × 11 × 20mm^3 were manufactured using the selective laser melting machines EOS M 270 and EOS M 290. Fig. 4 (b) shows an exemplary specimen preparation for measuring the melt pool width.

For AlSi10Mg 33 process parameters with 4 specimens each have been manufactured and measured. For 1.2709 5 process parameters with 4 specimens each have been manufactured and measured. Since Ti6Al4V has been taken from the literature [9] no statistic specimens are available.

Microscope images of the specimen micro-sections were conducted on a ZEISS Axioskop A1 HAL 100.

5. Results and discussion

In order to check suitability of Eq. (3), experiments are conducted using aluminum alloy AlSi10Mg and maraging steel 1.2709 as powder material. Measurements for titanium Ti6Al4 V were taken from the literature and included in the analysis [9]. The melt pool width b

Table 2
Material properties of the considered powder materials.

	λ [W/(K m)]	T [K]	ρ [kg/m^3]	c_p [J/(kg K)]
AlSi10Mg	140	870	2670	910
Ti6Al4 V	6.7	1933	4410	526.3
1.2709	15	1445	8050	450

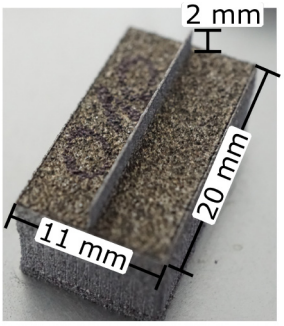

(a) Specimen geometry

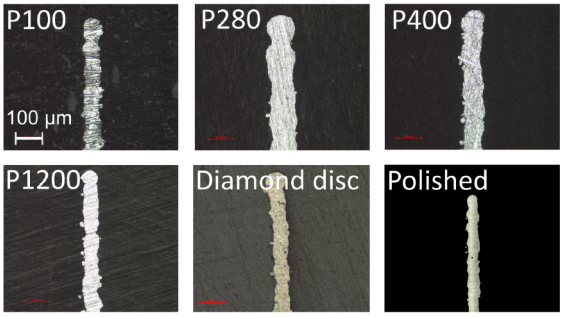

(b) Sandpaper and diamond disc polished melt track

Fig. 4. Specimen for melt track measurement.

is measured for varying laser power and scanning speed. The experimental data is depicted in Fig. 5 using a Π_u-Π_1 coordinate system. Despite some scattering, all data points collapse on one single curve as predicted by the theory according to Eq. (3). Measuring the width of the solidified material the results signify that the thermal strain can be neglected yielding a precise approximation. It is remarkable that on a coarse-grained scale neglecting the complex nature of the temperature or velocity distribution within the melt zone, just two dimensionless quantities suffice in order to characterize the dominant mechanisms underlying single-track formation. Furthermore, this significantly reduces the amount of experimental work: Instead of conducting experiments for varying scanning speed, laser power and material parameters, it is only necessary to vary the dimensionless parameter Π_1 either by scanning speed or laser power. To further interpret the results in Fig. 5, relevant time scales allowing for comparing different physical mechanisms are introduced. The diffusion time t_{diff},

$$t_{\mathrm{diff}} = \frac{\rho c_{\mathrm{p}} b^2}{\lambda}, \tag{5}$$

represents the characteristic time to transport heat over a characteristic length, that is, the melt pool width b, with the thermal diffusivity $k = \lambda/(\rho c_{\mathrm{p}})$. Since the melting process is modelled employing an open moving control volume, the convection time t_{conv} is introduced,

$$t_{\mathrm{conv}} = \frac{b}{v_{\mathrm{s}}}. \tag{6}$$

The convection time is a measure for the rate of energy flow into and out of the melt zone. Hence, the dimensionless parameter Π_u represents the ratio of convection time to diffusion time, $\Pi_u = t_{\mathrm{conv}}/t_{\mathrm{diff}}$. As observed in Fig. 5, the values of Π_u are smaller than 0.1 for Ti6Al4V and 1.2709 and between 0.1 and 0.5 for AlSi10Mg. Thus, during the melting process, energy flow into and out of the melt zone is dominated by convection mechanisms and not by heat transfer. Hence, in a first order approximation, the melting process can be modelled as adiabatic. Following this approach, dimensional analysis is carried out again, however, without taking into account the conductivity λ. Since the corresponding dimension matrix has rank 4, the single dimensionless product $\Pi = b^2 v_{\mathrm{s}} \rho c_{\mathrm{p}} \Delta T_{\mathrm{l}} / P_{\mathrm{L}}$ is derived. This yields the following simple scaling law for the melt pool width,

$$b = C \sqrt{\frac{P_{\mathrm{L}}}{v_{\mathrm{s}}}} \sqrt{\frac{1}{\rho c_{\mathrm{p}} \Delta T_{\mathrm{l}}}}, \tag{7}$$

where C is an unknown constant. The right-hand side of Eq. (7) allows for a direct physical interpretation: it represents the ratio between energy brought into the structure which in the literature is well-known as the line energy input $E_{\mathrm{L}} = P_{\mathrm{L}}/v_{\mathrm{s}}$ and the change of volume specific enthalpy $\rho c_{\mathrm{p}} \Delta T_{\mathrm{l}}$ consumed during phase transformation.

Before comparing the theoretical results to experimental findings, Eq. (7) is derived independently based on an averaged energy balance. On the one hand, this further indicates validity of the scaling law based on dimensional analysis and on the other hand allows for specification of the unknown constant C in Eq. (7). An averaged energy balance is formulated employing a non-material control volume moving with the scanning speed v_s as depicted in Fig. 6.

Thus, the control volume represents an open system with a mass flux entering and leaving through the surface of the control volume. The employed control volume is chosen in such a way that unmelted powder particles enter and liquid material leaves the system, cf. Fig. 6. According to Müller [21] the general balance equation for a generic quantity ψ for an open system moving with the velocity $\underline{v}$ (velocity vector) reads:

$$\frac{\mathrm{D}}{\mathrm{D}t} \int_{\Omega} \rho \psi \mathrm{d}V = -\int_{\partial\Omega} \rho \psi \underline{w} \cdot \underline{n} \mathrm{d}A + \int_{\partial\Omega} \underline{\theta} \cdot \underline{n} \mathrm{d}A + \int_{\Omega} \sigma \mathrm{d}V. \tag{8}$$

The first surface integral on the right-hand side represents the convective flux with the relative velocity $\underline{w}$ between material particles and the velocity of the moving control volume. Furthermore, $\underline{\theta}$ represents the non-convective flux and σ is a source density. Applied to the present case of an open system moving with velocity $\underline{v}_s$ under adiabatic conditions, the general energy balance is given by:

$$\frac{\mathrm{D}}{\mathrm{D}t} \int_{\Omega} \rho e \mathrm{d}V = \int_{\partial\Omega} \rho e \underline{v}_s \cdot \underline{n} \mathrm{d}A + \alpha P_L. \tag{9}$$

Here, e is the thermal energy density and α is the material's absorptivity. The significant advantage of using a control volume moving at scanning speed is that the melting process appears as quasi-stationary since two states at different points in time are undistinguishable. Thus the left-hand side of Eq. (9) vanishes. Employing the caloric equation of state for the solid and liquid phase and introducing $\bar{(\cdot)}_{\mathrm{out}}$ and $\bar{(\cdot)}_{\mathrm{in}}$ as averaged quantities over the inlet and outlet surfaces, respectively, the energy balance can be rewritten in the form

$$\left((\rho \bar{c_{\mathrm{p}}} T)_{\mathrm{out}} A_{\mathrm{out}} - (\rho \bar{c_{\mathrm{p}}} T)_{\mathrm{in}} A_{\mathrm{in}} \right) = \alpha P_L. \tag{10}$$

Further, the melt pool is assumed to have a circular cross-section and is self-similar: the depth of the melt pool is proportional to the width b implying $A_{\mathrm{in}} = A_{\mathrm{out}} = \xi b^2$ with the proportionality constant ξ. In addition, in a first-order approximation, it is supposed that $\bar{\rho}_{\mathrm{in}} \approx \bar{\rho}_{\mathrm{out}} = \bar{\rho}$ and $\bar{c}_{\mathrm{p,in}} \approx \bar{c}_{\mathrm{p,out}} = \bar{c}_{\mathrm{p}}$. Incorporating the

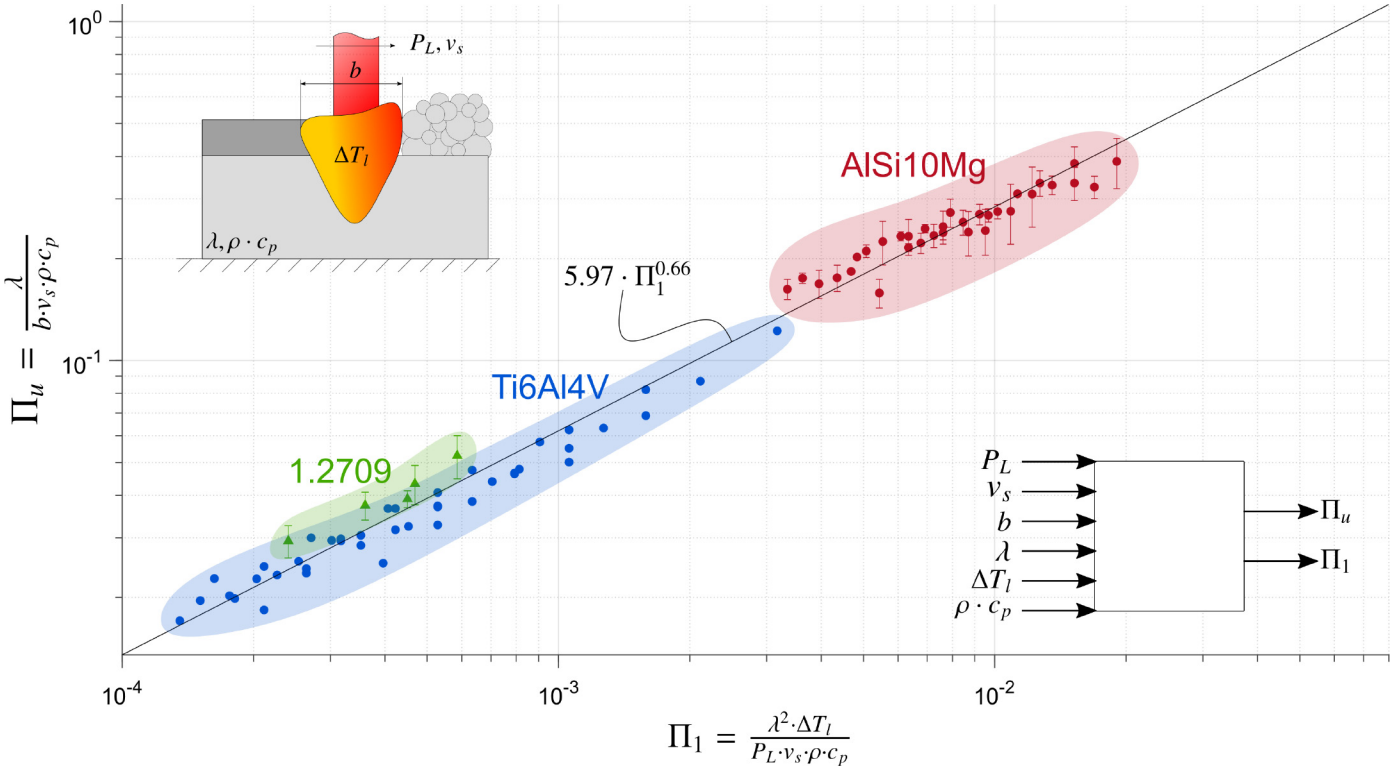

Fig. 5. Dimensionless parameters obtained by means of dimensional analysis for specimens machined on an EOS SLM machine with aluminum AlSi10Mg, titanium Ti6Al4V and maraging steel 1.2709.

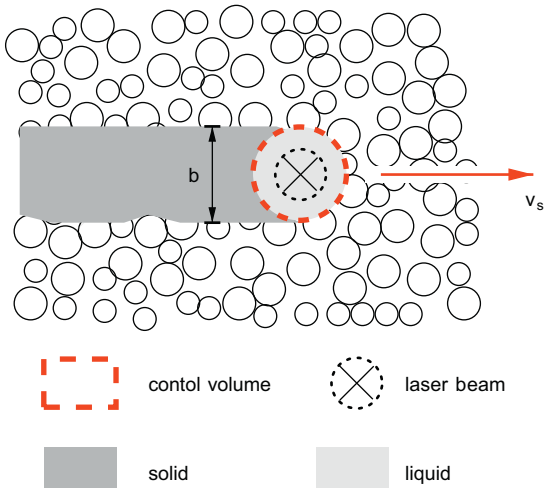

Fig. 6. Energy balance for a non-material control volume moving with the scanning speed v_s.

aforementioned assumption into the energy balance yields the same results as Eq. (7):

$$b = \sqrt{\frac{\alpha}{\xi}}\sqrt{\frac{P_L}{v_s}}\sqrt{\frac{1}{\rho c_p \Delta T_l}}. \tag{11}$$

This shows, that the unknown constant in Eq. (7) depends on the shape of the melting zone through the geometry factor ξ as well as on the materials absorptivity α.

The theoretical results according to Eq. (11) are now validated against experimental data provided by the authors. Fig. 7 shows the measurements of melt zone width b with respect to the line energy $E_L = P_L/v_s$. The experimental data is in a very good agreement with the theory, predicting that the width b scales with the square root of the line energy. Although heat conduction effects are more pronounced for AlSi10Mg compared to 1.2709 and Ti6Al4V, the proposed scaling law still holds. For the calculation of the shape factor ξ is not straight-forward without using numerical methods, the constant C has been calculated using regression analysis. The observed dependency of C on the employed material indicates different material absorptivity and melt pool shapes. Hence, for application purposes it is more feasible to reduce the obtained scaling-law to its simplest form:

$$b \propto \sqrt{E_L}. \tag{12}$$

Table 3
Proportionality constant C for the investigated materials.

	AlSi10Mg	Ti6Al4V	1.2709
C	0.49	0.64	0.58

The corresponding proportionality constant can then be determined for a given material employing one experiment. For the materials investigated here, Table 3 summarises the determined constants C for Eq. (12).

Coming back to the empirical data shown in Fig. 2, the obtained scaling law allows for adequately predicting the lattice strut thickness with respect to the line energy E_L in the sound surface regime.

6. Conclusion

In summary, using dimensional analysis as well as averaged energy balance, it was shown that a scaling law adequately predicts the width of the melt pool with respect of the most important process as well as material parameters of the powder. The scaling law has been derived based on a first order modelling approach of the melting process which is valid for a certain region of the process window. Numerous experiments have been conducted by the authors employing titanium Ti6Al4V, maraging steel 1.2709 and aluminum AlSi10Mg as powder material, respectively. It has been shown that the melt pool width scales according to $b \propto \sqrt{E_L}$ as predicted by the theory. The derived scaling law interconnects the process parameters with macroscopic as well as mesoscopic characteristics of a lattice structure. This serves as a basis for laser driven design of thin-walled lattice structures manufactured by contour exposure where the melt pool width b controls the relative density of the lattice and thus the overall elastic properties. In future works, additional effects such as surface tension of the melt pool that leads to part porosity (due to pronounced Marangoni convection) or strut waviness (due to Plateau-Rayleigh instability) need to be examined. For contour and hatch-exposure using more melt tracks the hatch distance d_h needs to be considered in order to assess dense parts. While the present work only considers the melt pool width, the same methodology needs to be conducted for the melt pool depth in future studies to determine whether keyhole or surface welding is present. Finally, machine specific quantities such as laser beam diameter may be incorporated to provide a machine independent predictive framework.

CRediT authorship contribution statement

Alexander Großmann: Conceptualization, Supervision, Writing - review & editing. **Julian Felger:** Formal analysis, Writing -

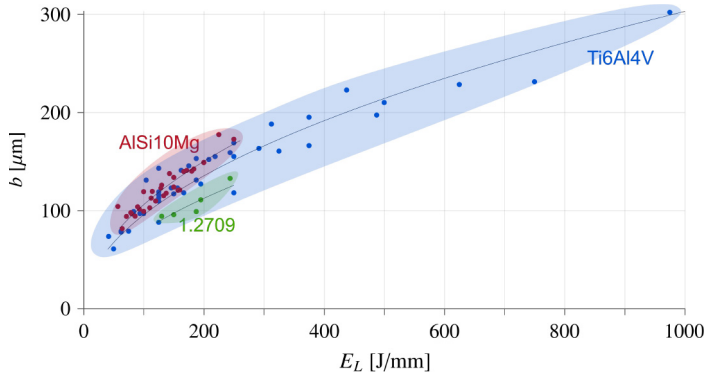

Fig. 7. Correlation between melt pool width and line energy for AlSi10Mg, Ti6Al4 V and 1.2709.

review & editing. **Tilman Frölich:** Investigation, Visualization. **Julian Gosmann:** Visualization. **Christian Mittelstedt:** Writing - review & editing.

References

[1] G.I. Barenblatt, Scaling, Cambridge University Press, Cambridge, 2003.
[2] J. Bauer, A. Schroer, R. Schwaiger, O. Kraft, Approaching theoretical strength in glassy carbon nanolattices, Nat. Mater. 15 (4) (2016) 438–443.
[3] C. Bonatti, D. Mohr, Large deformation response of additively-manufactured FCC metamaterials: from octet truss lattices towards continuous shell mesostructures, Int. J. Plast. 92 (2017) 122–147. https://doi.org/10.1016/j.ijplas.2017.02.003.
[4] D. Buchbinder, H. Schleifenbaum, S. Heidrich, W. Meiners, J. Bültmann, High power selective laser melting (HP SLM) of aluminum parts, Phys. Procedia 12 (2011) 271–278. https://doi.org/10.1016/j.phpro.2011.03.035.
[5] F. Calignano, M. Lorusso, J. Pakkanen, F. Trevisan, E.P. Ambrosio, D. Manfredi, P. Fino, Investigation of accuracy and dimensional limits of part produced in aluminum alloy by selective laser melting, Int. J. Adv. Manuf. Technol. 88 (1-4) (2017) 451–458. https://doi.org/10.1007/s00170-016-8788-9.
[6] Y. Chen, T. Li, Z. Jia, F. Scarpa, C.-W. Yao, L. Wang, 3D printed hierarchical honeycombs with shape integrity under large compressive deformations, Mater. Des. 137 (2018) 226–234. https://doi.org/10.1016/j.matdes.2017.10.028.
[7] B.G. Compton, J.A. Lewis, 3D-printing of lightweight cellular composites, Advanced materials (Deerfield Beach, Fla.) 26 (34) (2014) 5930–5935. https://doi.org/10.1002/adma.201401804.
[8] C. Emmelmann, P. Sander, J. Kranz, E. Wycisk, Laser additive manufacturing and bionics: redefining lightweight design, Phys. Procedia 12 (2011) 364–368. https://doi.org/10.1016/j.phpro.2011.03.046.
[9] H. Gong, G. Hengfeng, K. Zeng, J. Dilip, D. Pal, B. Stucker, D. Christiansen, J. Beuth, J.J. Lewandowski, Melt pool characterization for selective laser melting of Ti-6Al-4V pre-alloyed powder, Proceedings of the Solid Freeform Fabrication Symposium (2014) 256–267.
[10] D.B. Hann, J. Iammi, J. Folkes, A simple methodology for predicting laser-weld properties from material and laser parameters, J. Phys. D. Appl. Phys. 44 (44) (2011) 445401. https://doi.org/10.1088/0022-3727/44/44/445401.
[11] J.A. Harris, R.E. Winter, G.J. McShane, Impact response of additively manufactured metallic hybrid lattice materials, Int. J. Impact Eng. 104 (2017) 177–191. https://doi.org/10.1016/j.ijimpeng.2017.02.007.
[12] T. Heeling, M. Cloots, K. Wegener, Melt pool simulation for the evaluation of process parameters in selective laser melting, Addit. Manuf. 14 (2017) 116–125. https://doi.org/10.1016/j.addma.2017.02.003.
[13] S.A. Khairallah, A.T. Anderson, A. Rubenchik, W.E. King, Laser powder-bed fusion additive manufacturing: physics of complex melt flow and formation mechanisms of pores, spatter, and denudation zones, Acta Mater. 108 (2016) 36–45. https://doi.org/10.1016/j.actamat.2016.02.014.
[14] W.E. King, H.D. Barth, V.M. Castillo, G.F. Gallegos, J.W. Gibbs, D.E. Hahn, C. Kamath, A.M. Rubenchik, Observation of keyhole-mode laser melting in laser powder-bed fusion additive manufacturing, J. Mater. Process. Technol. 214 (12) (2014) 2915–2925. https://doi.org/10.1016/j.jmatprotec.2014.06.005.
[15] S. Kolossov, E. Boillat, R. Glardon, P. Fischer, M. Locher, 3D FE simulation for temperature evolution in the selective laser sintering process, Int. J. Mach. Tool Manuf. 44 (2-3) (2004) 117–123. https://doi.org/10.1016/j.ijmachtools.2003.10.019.
[16] H. Lei, C. Li, J. Meng, H. Zhou, Y. Liu, X. Zhang, P. Wang, D. Fang, Evaluation of compressive properties of SLM-fabricated multi-layer lattice structures by experimental test and μ-CT-based finite element analysis, Mater. Des. 169 (2019) 107685. https://doi.org/10.1016/j.matdes.2019.107685.
[17] C.L.A. Leung, S. Marussi, R.C. Atwood, M. Towrie, P.J. Withers, P.D. Lee, In situ X-ray imaging of defect and molten pool dynamics in laser additive manufacturing, Nat. Commun. 9 (1) (2018) 1355. https://doi.org/10.1038/s41467-018-03734-7.
[18] R. Li, J. Liu, Y. Shi, L. Wang, W. Jiang, Balling behavior of stainless steel and nickel powder during selective laser melting process, Int. J. Adv. Manuf. Technol. 59 (9-12) (2012) 1025–1035. https://doi.org/10.1007/s00170-011-3566-1.
[19] L.R. Meza, S. Das, J.R. Greer, Strong, lightweight, and recoverable three-dimensional ceramic nanolattices, Science (345) (2014) 1322–1326. https://doi.org/10.1126/science.1255908.
[20] T.M. Mower, M.J. Long, Mechanical behavior of additive manufactured, powder-bed laser-fused materials, Mater. Sci. Eng., A 651 (2016) 198–213. https://doi.org/10.1016/j.msea.2015.10.068.
[21] I. Müller, W.H. Müller, Fundamentals of Thermodynamics and Applications: With Historical Annotations and Many Citations From Avogadro to Zermelo, Springer Berlin Heidelberg, Berlin, Heidelberg, 2009, http://sub-hh.ciando.com/book/?bok_id=28775.
[22] T. Niendorf, F. Brenne, M. Schaper, Lattice structures manufactured by SLM: on the effect of geometrical dimensions on microstructure evolution during processing, Metall. Mater. Trans. B 45 (4) (2014) 1181–1185. https://doi.org/10.1007/s11663-014-0086-z.
[23] E.O. Olakanmi, R.F. Cochrane, K.W. Dalgarno, A review on selective laser sintering/melting (SLS/SLM) of aluminium alloy powders: processing, microstructure, and properties, Prog. Mater. Sci. 74 (2015) 401–477. https://doi.org/10.1016/j.pmatsci.2015.03.002.
[24] R. Rai, J.W. Elmer, T.A. Palmer, T. DebRoy, Heat transfer and fluid flow during keyhole mode laser welding of tantalum, Ti-6Al-4V, 304L stainless steel and vanadium, J. Phys. D Appl. Phys. 40 (18) (2007) 5753–5766. https://doi.org/10.1088/0022-3727/40/18/037.
[25] O. Rehme, C. Emmelmann, M.M. Morlock, Cellular Design for Laser Freeform Fabrication: Zugl.: Hamburg-Harburg, Techn. Univ., Inst. für Laser- und Anlagensystemtechnik, Diss., 2009, first ed.,Schriftenreihe Lasertechnik. 4. Cuvillier Göttingen. 2010.
[26] S.L. Sing, F.E. Wiria, W.Y. Yeong, Selective laser melting of lattice structures: a statistical approach to manufacturability and mechanical behavior, Robot. Comput. Integr. Manuf. 49 (2018) 170–180. https://doi.org/10.1016/j.rcim.2017.06.006.
[27] S.L. Sing, F.E. Wiria, W.Y. Yeong, Selective laser melting of titanium alloy with 50 wt% tantalum: effect of laser process parameters on part quality, Int. J. Refract. Met. Hard Mater. 77 (2018) 120–127. https://doi.org/10.1016/j.ijrmhm.2018.08.006.
[28] J. Souza, A. Großmann, C. Mittelstedt, Micromechanical analysis of the effective properties of lattice structures in additive manufacturing, Addit. Manuf. 23 (2018) 53–69. https://doi.org/10.1016/j.addma.2018.07.007.
[29] N. Takata, H. Kodaira, A. Suzuki, M. Kobashi, Size dependence of microstructure of AlSi10Mg alloy fabricated by selective laser melting, Mater. Charact. 143 (2018) 18–26. https://doi.org/10.1016/j.matchar.2017.11.052.
[30] T. Tancogne-Dejean, M. Diamantopoulou, M.B. Gorji, C. Bonatti, D. Mohr, 3D plate-lattices: an emerging class of low-density metamaterial exhibiting optimal isotropic stiffness, Advanced materials (Deerfield Beach, Fla.) 30 (45) (2018) 1803334. https://doi.org/10.1002/adma.201803334.
[31] T. Tancogne-Dejean, A.B. Spierings, D. Mohr, Additively-manufactured metallic micro-lattice materials for high specific energy absorption under static and dynamic loading, Acta Mater. 116 (2016) 14–28. https://doi.org/10.1016/j.actamat.2016.05.054.
[32] S. van Bael, G. Kerckhofs, M. Moesen, G. Pyka, J. Schrooten, J.P. Kruth, Micro-CT-based improvement of geometrical and mechanical controllability of selective laser melted Ti6Al4V porous structures, Mater. Sci. Eng. A 528 (24) (2011) 7423–7431. https://doi.org/10.1016/j.msea.2011.06.045.
[33] B. van Hooreweder, J.-P. Kruth, Advanced fatigue analysis of metal lattice structures produced by selective laser melting, CIRP Ann. 66 (1) (2017) 221–224. https://doi.org/10.1016/j.cirp.2017.04.130.
[34] Association of German Engineers (VDI), VDI Guideline 3405 Part 3 / Additive manufacturing processes, rapid manufacturing / Design rules for part production using laser sintering and laser beam melting, Beuth, Düsseldorf, December 2015.
[35] Z. Wang, T.A. Palmer, A.M. Beese, Effect of processing parameters on microstructure and tensile properties of austenitic stainless steel 304L made by directed energy deposition additive manufacturing, Acta Mater. 110 (2016) 226–235. https://doi.org/10.1016/j.actamat.2016.03.019.
[36] P. Wei, Z. Wei, Z. Chen, Y. He, J. Du, Thermal behavior in single track during selective laser melting of AlSi10Mg powder, Appl. Phys. A 123 (9) (2017) 133. https://doi.org/10.1007/s00339-017-1194-9.
[37] B. Xiao, Y. Zhang, Laser sintering of metal powders on top of sintered layers under multiple-line laser scanning, J. Phys. D Appl. Phys. 40 (21) (2007) 6725–6734. https://doi.org/10.1088/0022-3727/40/21/036.
[38] L.P. Yarin, The Pi-Theorem, Springer Berlin Heidelberg, Berlin, Heidelberg, 2012. https://doi.org/10.1007/978-3-642-19565-5.